

# EFFECT OF COOLING RATE ON MICROSTRUCTURE AND MECHANICAL PROPERTIES OF AA5056 Al-Mg ALLOY

M. Asl Zare and R. Taghiabadi 

Department of Materials Science and Metallurgy, Imam Khomeini International University, Qazvin, Iran

M. H. Ghoncheh

Department of Mechanical Engineering, University of New Brunswick, Fredericton, NB, Canada

Copyright © 2021 American Foundry Society  
<https://doi.org/10.1007/s40962-021-00704-6>

## Abstract

*This study investigates the effect of different solidification cooling rates (0.5, 7.5, 13.5, 57.5, and 85 °C/s) on the solidification parameters, microstructure evolution, and mechanical properties of AA5056 Al-Mg alloy. According to the results, augmenting the cooling rate lowered the solidification time, and due to high thermal undercooling, substantially refined the microstructure. For instance, increasing the cooling rate from about 0.5 to about 85 °C/s decreased the fraction of  $Al_3Mg_2$ ,  $Mg_2Si$ , and Fe-rich compounds by 58, 64, and 27%, respectively. It also substantially refined the grains, reduced the size of secondary dendrite arm spacing (SDAS), and lowered the porosity*

*content from about 3.8% to about 0.3%. The hardness, tensile strength, and fracture strain of the alloy increased by 44%, 140%, and 395%, respectively, as the cooling rate increased from 0.5 to 85 °C/s. The fracture mechanism also changed from a brittle-dominated mode to a high-energy ductile mode comprising of extensive dimpled zones at the higher cooling rates.*

**Keywords:** Al-Mg, AA5056, solidification cooling rate, thermal analysis, mechanical properties

## Introduction

Due to its high specific strength/stiffness, excellent formability, good weldability, and outstanding weather/saltwater corrosion resistance, AA5056 Al-Mg alloy has a great potential to be used in aerospace, automotive, and marine industries.<sup>1,2</sup> Therefore, some efforts have been made so far to improve the mechanical properties of AA5056 alloy.

Considering the easy formation of shear bands in its structure, AA5056 alloy exhibits high potential for strain-induced microstructural refinement through severe plastic deformation (SPD).<sup>3</sup> The positive impact of equal channel angular pressing and equal channel angular extrusion on the mechanical properties of AA5056 alloy has been demonstrated.<sup>3,4</sup> The semi-solid processing, including rheoforming and thixoforming, can be also employed to

fabricate Al-Mg parts with excellent mechanical properties.<sup>5,6</sup> However, these processes are cost intensive, require especial dies/equipment, and need a high degree of control over the process. Moreover, the SPD processes encounter with the sample size and shape limitations, and impair the alloy ductility.

Chemical modification can be also used to improve the mechanical properties of Al-Mg alloys.<sup>7,8</sup> However, it may produce metallurgical issues such as oxidation loss of the modifier element(s), formation of unwanted compounds, and increasing the porosity content.<sup>9,10</sup> The homogenization treatment is another approach to modify the microstructure, improve the efficiency of subsequent formation processes, and enhance the mechanical properties/formability of Al-Mg alloys.<sup>11,12</sup> However, this process cannot heal the existing defects such as micropores and due to its time- and energy-consuming nature, may encounter with economic limitations.

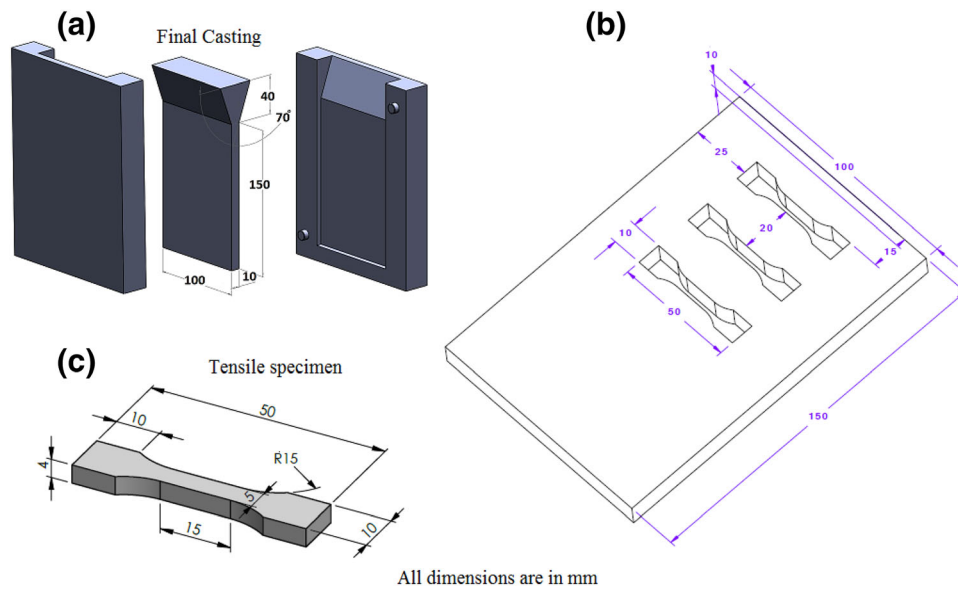


**Figure 1. Schematic diagrams showing dimensions and geometry of (a) mold/final casting, (b) tensile test sampling location, and (c) tensile test sample.**

Increasing the cooling rate during solidification is another way to modify the as-cast microstructure of alloys. High cooling rate decreases the size, changes the morphology, and promotes more uniform distribution of microconstituents/micropores within the matrix. It also decreases the size of SDAS, refines the grains, and reduces micro-segregations.<sup>12–15</sup> Therefore, it is thought to be a promising approach for simultaneous improvement of mechanical strength and ductility. On this basis, the effect of cooling rate on Al-Mg alloys has been the subject of many studies. According to the results, increasing the cooling rate substantially improves the mechanical properties, but the final result is a function of Mg content in the alloy where the mechanical properties of moderate-to-high Mg-bearing alloys such as AA 5056 alloy is more sensitive to the cooling rate.<sup>15–18</sup>

AA 5056 alloy is known as the strongest non-heat-treatable Al alloy which due to its high ductility and excellent formability is a promising candidate for the fabrication of wide variety of components such as honeycomb cores in aircraft floors, aircraft leading, and trailing edges, fan casing, fuel cells, helicopter rotor blades, fasteners, navy bulkhead joiner panels.<sup>19,20</sup> However, to the best of our knowledge no reports are available on the effect of cooling rate on its microstructure and mechanical properties. Therefore, improving its mechanical properties by increasing the solidification cooling rate seems a new research topic. The computer-aided thermal analysis of cooling curves was also performed in the current research to monitor the alloy behavior during the solidification process.

**Table 1. Coding System and Average Cooling Rates of the Molds Used in the Present Study**

	Silica	Mild steel	Mild steel (water-cooled)	Copper	Copper (water-cooled)
Ave. cooling rate (°C/s)	0.5	7.5	13.5	57.5	85
Code	SC	ST	STW	CU	CUW

## Materials and Methods

The as-received AA5056 Al-Mg alloy with the composition of 5.01Mg-0.28Si-0.2Fe-0.12Mn (mass fraction, %) was re-melted in a clay-graphite crucible using an electrical resistance furnace. The melt was kept at 750 °C for 10 min followed by degassing using dry C<sub>2</sub>Cl<sub>6</sub> tablets. It was then skimmed and gently stirred before being poured at 720 °C into the molds with identical geometries (Figure 1a) made from different materials to simulate different cooling rates (Table 1).

Thermal analysis was performed by inserting a K-type thermocouple into the mold wall, where its tip was about 25 mm above the mold bottom. The thermocouple was connected to a high-speed data acquisition system equipped with an analog-to-digital convertor with a resolution of 0.0015% and response time of 0.02 s to record the melt temperature variation during the solidification.

The Vickers microhardness of the samples was determined under the load of 500 g and dwelling time of 15 s according to the ASTM E384-05A. The  $\alpha$ -Al matrix microhardness was also measured by the same tester under the load of 5 g and dwelling time of 15 s. The reported final value is the average of eight measurements. The subsize tensile samples were extracted from the cast slabs based on a scaled-down version of the ASTM E8 (Figure 1b)<sup>21</sup> and tested using a Zwick/Roell tensile testing machine at the constant crosshead speed of 0.5 mm/min, and the average of four results is reported as the final value.

Standard procedures were used to prepare the metallography samples. Each cross section was etched using a 2% HF solution for 10 s to reveal its microstructure. The grain structure was revealed by Tucker's reagent. A scanning electron microscope (SEM) coupled with an energy-

dispersive spectroscopy (EDS) was employed to study the microstructures and perform phase microanalysis. An optical microscope (OM) coupled with a portrait image analysis system (Clemex Vision, PE) was used for image analysis. The grain size was determined based on ASTM E112-12 using the linear intercept method. To porosity content of samples was also determined using Archimedes' method.<sup>22</sup>

## Results and Discussion

### Microstructural Characterization

Figure 2a shows the microstructure of AA5056 alloy solidified under the cooling rate of 0.5 °C/s (SC sample). According to the Al-Mg-Si-Fe phase distribution map

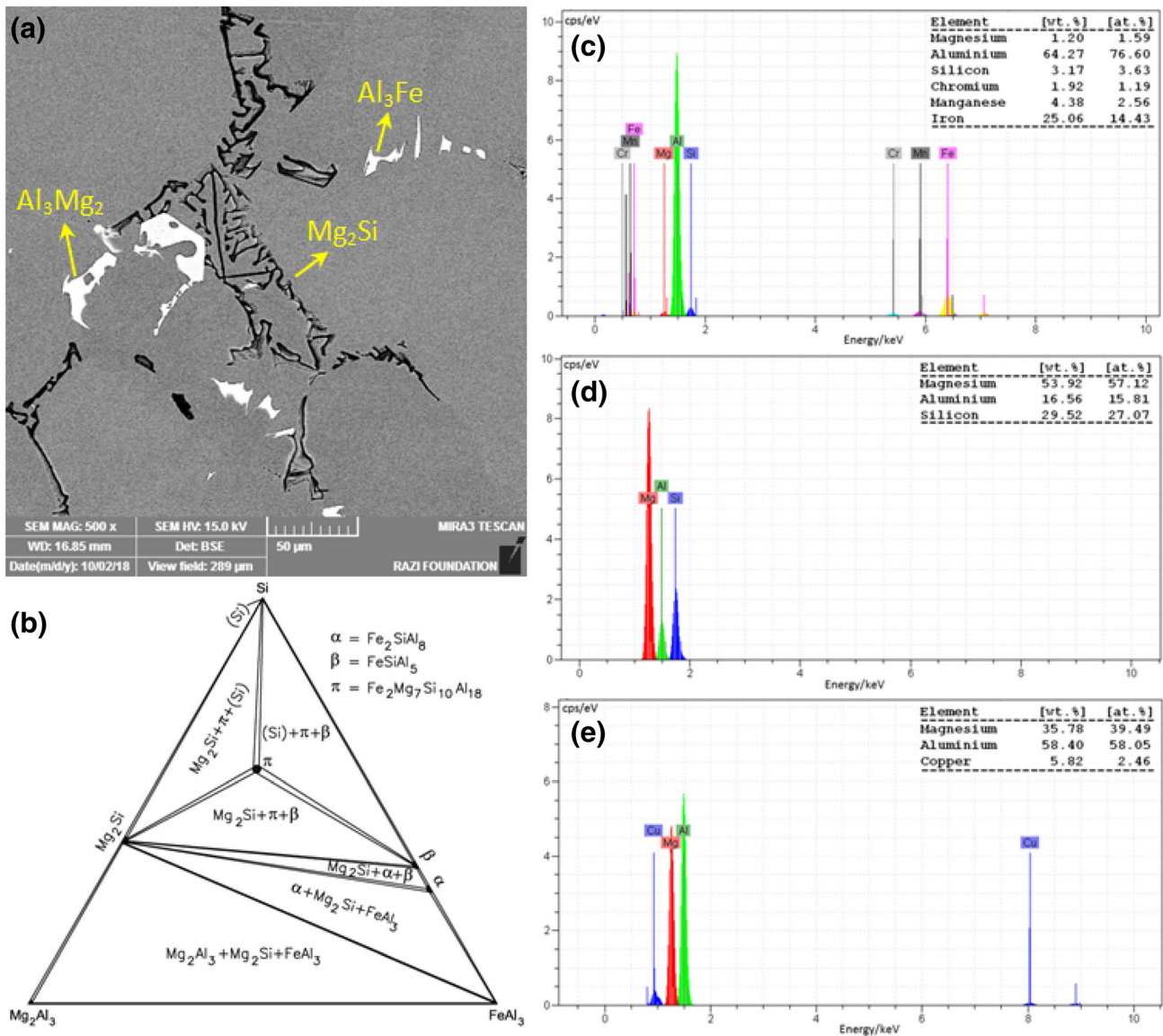


Figure 2. (a) SEM microstructure of AA5056 alloy at the cooling rate of 0.5 °C/s (SC sample), (b) Al-Mg-Si-Fe phase distribution map in the solid state<sup>23</sup>, (c–e) EDS analysis of the marked phases in (a).

(Figure 2b)<sup>23</sup> and EDS microanalysis results (Figure 2c-e), the main phases present in the microstructure are light gray  $\text{Al}_3\text{Mg}_2$ , black  $\text{Mg}_2\text{Si}$ , and white  $\text{Al}_3\text{Fe}$  which are embedded in the dark gray  $\alpha\text{-Al}$  matrix. The formation of Fe-rich compounds can be explained by the existence of Fe impurity in the chemical analysis of the as-received alloy.

According to Figure 3, augmenting the cooling rate substantially refined the second phases and encouraged their even distribution within the matrix of AA5056 alloy. Based on the image analysis results shown in Table 2, increasing the cooling rate from about 0.5 to about 85 °C/s decreased the fraction of  $\text{Al}_3\text{Mg}_2$  by 58%,  $\text{Mg}_2\text{Si}$  by 64%, and Fe-rich compounds by 27%. The high cooling rate also substantially refined the grains (Figures 4a and 5) and reduced the size of SDAS (Figure 4b).

The microstructure refinement as a result of high cooling rate can be ascribed to the larger thermal undercooling developed during the solidification, which decreases the nuclei critical size, increases the nucleation driving force, and restricts the

diffusion-controlled transformations required for the growth stage.<sup>24,25</sup> Then a large number of crystals nucleated on or in vicinity of the metallic mold walls, especially those with higher cooling rate, can be dissociated into the melt and, depending on their survival rate, cause grain multiplication and refinement of the structure.<sup>26,27</sup> Increasing the thermal

**Table 2. Effect of Cooling Rate on the Area Fraction of  $\text{Al}_3\text{Mg}_2$ ,  $\text{Mg}_2\text{Si}$ , Fe-Rich Compounds and Volume Fraction of Porosities**

Cooling rate ( °C/s)	Area fraction (%)			Volume fraction (%)
	$\text{Al}_3\text{Mg}_2$	$\text{Mg}_2\text{Si}$	Fe-rich compounds	
0.5	1.81±0.21	0.59±0.08	0.47±0.06	3.81
7.5	1.14±0.16	0.36±0.06	0.40±0.04	1.07
13.5	1.04±0.17	0.29±0.04	0.37±0.03	0.89
57.5	0.90±0.08	0.27±0.03	0.36±0.04	0.38
85	0.75±0.07	0.21±0.03	0.34±0.02	0.32

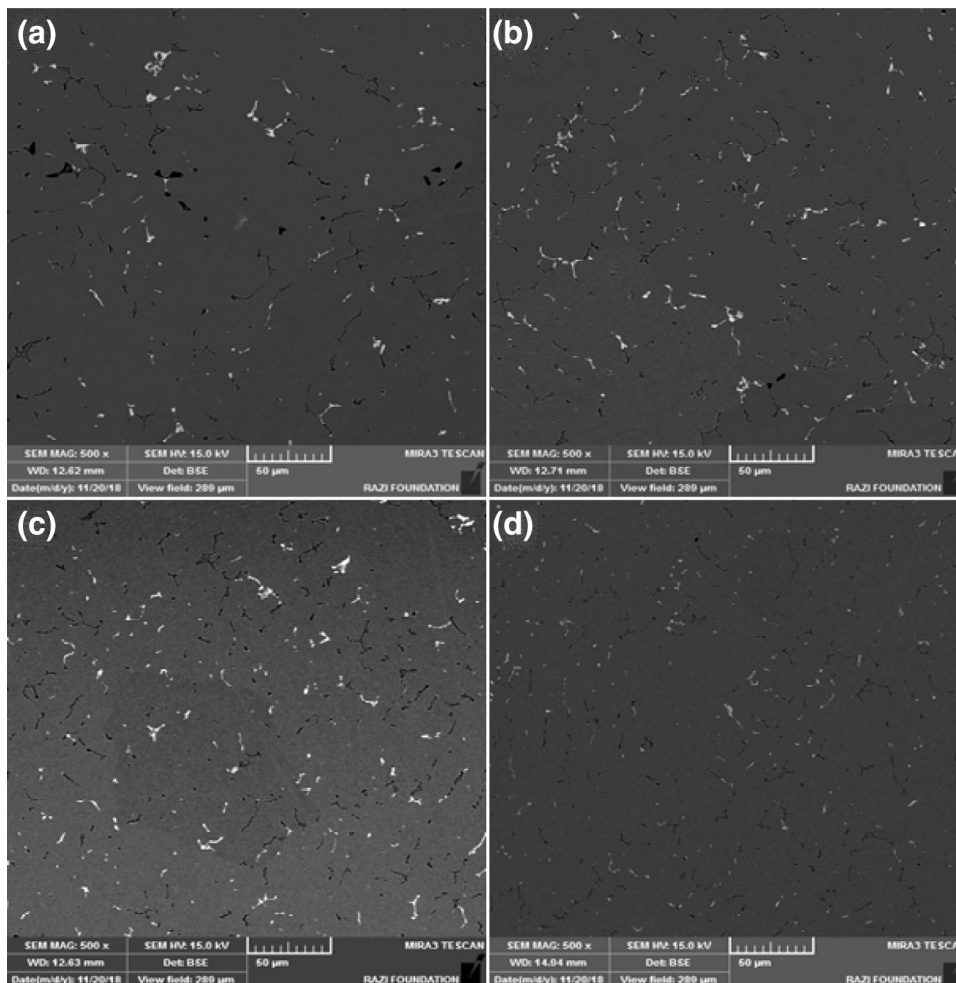


**Figure 3. Microstructure of AA5056 alloy solidified at the cooling rate of (a) 7.5 °C/s (ST sample), (b) 13.5 °C/s (STW sample), (c) 57.5 °C/s (CU sample), and (d) 85 °C/s (CUW sample).**



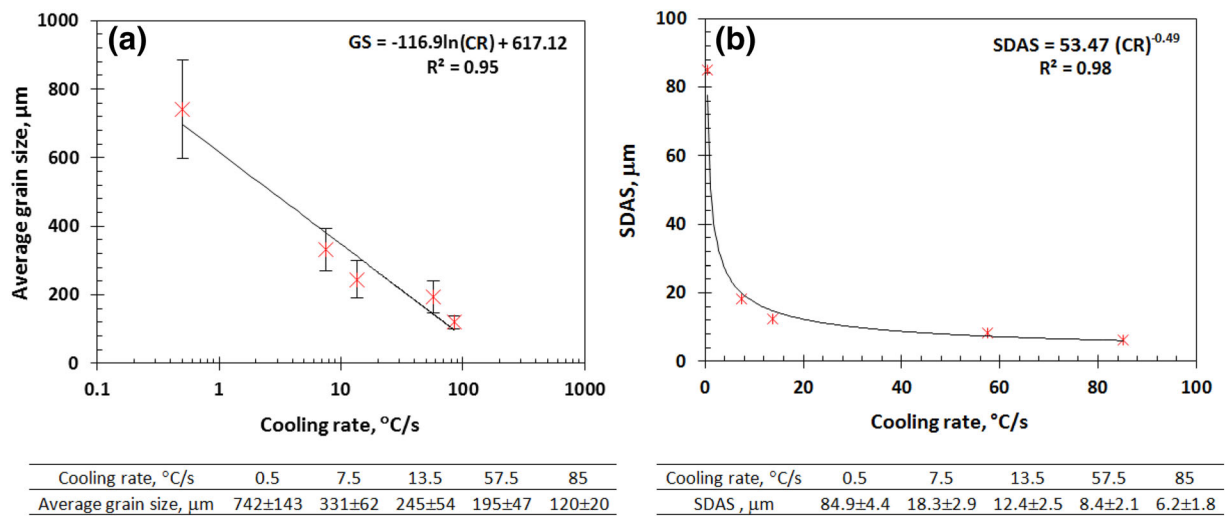


Figure 4. Effect of cooling rate on (a) grain size and (b) SDAS of AA5056 alloy.

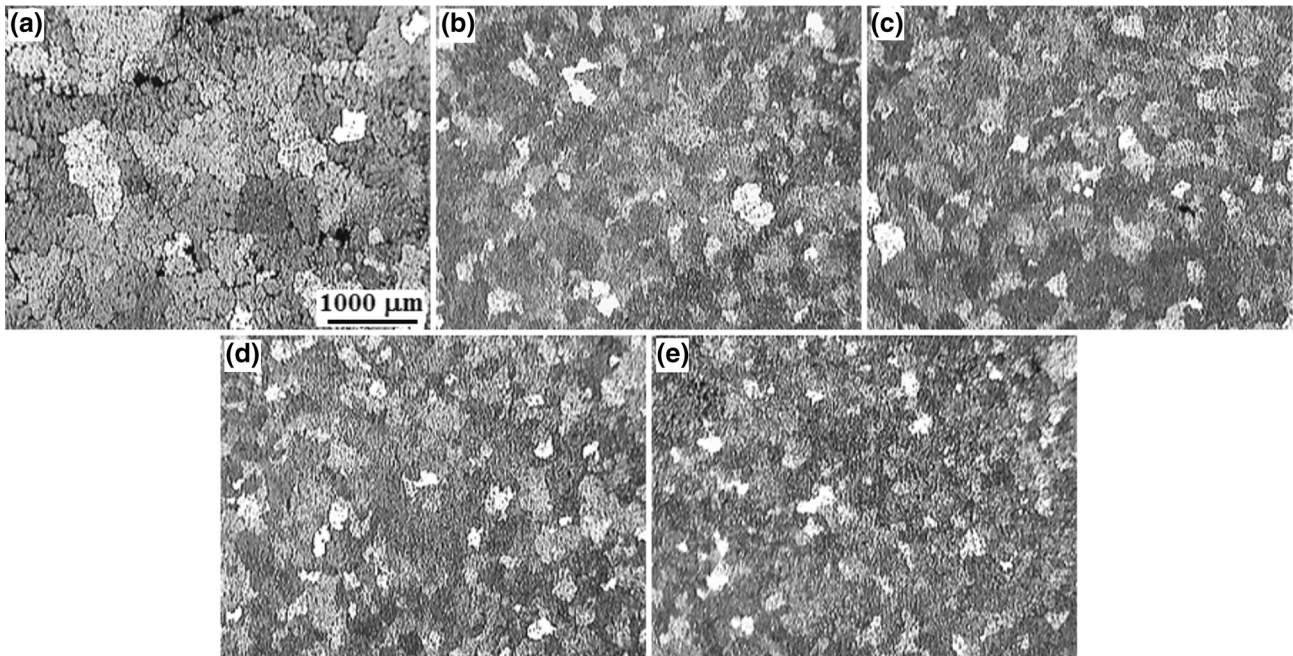


Figure 5. Effect of cooling rate on the grain morphology of AA5056 alloy.

undercooling also refined the grains by encouraging the additional nucleation within the constitutional undercooled zone ahead of solid-liquid interface.<sup>28</sup> The chance of coalescence and/or settling of the effective nucleation substrates is also reduced by the cooling rate.<sup>25</sup>

Increasing the cooling rate also substantially decreases the SDAS where its average value reduced from about 85 μm in ST sample to about 6 μm in CUW sample (Figure 4b). The relationship between SDAS solidification cooling rate can be expressed by the following equation<sup>29–31</sup>:

$$SDAS = a(CR)^{-b}$$

$$b = 0.3 - 0.5 \quad \text{Eqn. 1}$$

where, a and b are characteristic constant of each alloy. Considering the equation of the fitted power curve on data points in Figure 4b, it seems that the obtained results are well consistent with previous reports.<sup>31–33</sup> The reduction in SDAS as the cooling rate increase can be preliminary ascribed to the formation of more secondary dendrite arms on the primary stems. However, it also seems that the increased solid-liquid interface speed necessitates the higher area-to-volume ratio of dendrite arms to enhance the heat extraction.<sup>32</sup>

Lower porosity content is another benefit of solidification under a high cooling rate where the fraction of micropores decreases from about 3.8% in the SC sample to about 0.3% in CUW alloy. This is seemingly due to the combined

effect of several factors the most important of which are: (1) lower chance of hydrogen atoms for accumulation and development of gas micropores at hydrogen trapping sites, (2) less time available for the growth of gas pores, (3) lower volumetric porosity content through refining the grains and, consequently, lower size of liquid pockets at grain boundaries/interdendritic regions, (4) higher supersaturation level of hydrogen in the solidified portion of alloy, and as a result, less hydrogen is available for the growth of already-nucleated gas pores, and (5) less time

available for unfurling/inflation of entrained double oxides (as potential sites for hydrogen pores nucleation).<sup>25,34,35</sup>

### Thermal Analysis

Figure 6 shows the cooling and first derivative curves of the AA5056 alloy solidified under various cooling rates. In Figure 6a-d, N and S on each cooling curve represent the nucleation and solidus points. The interval between them is

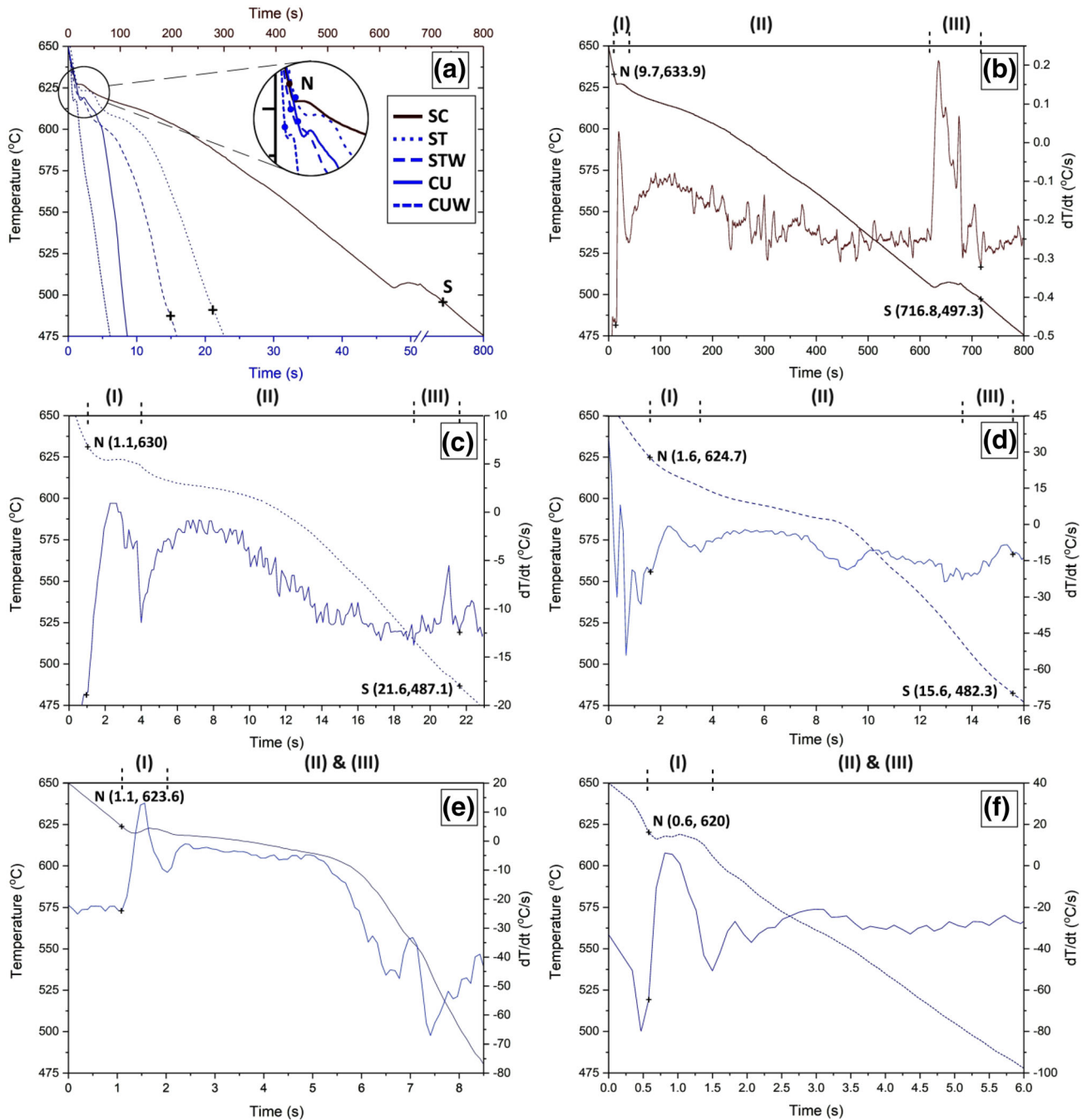


**Figure 6.** (a) A layout of cooling curves at various cooling rates, and derivative curve of (b) SC, (c) ST, (d) STW, (e) CU, and (f) CUW samples (note that solidus temperatures in CU and CUW samples were immeasurable due to rapid heat extraction from the solidifying system).

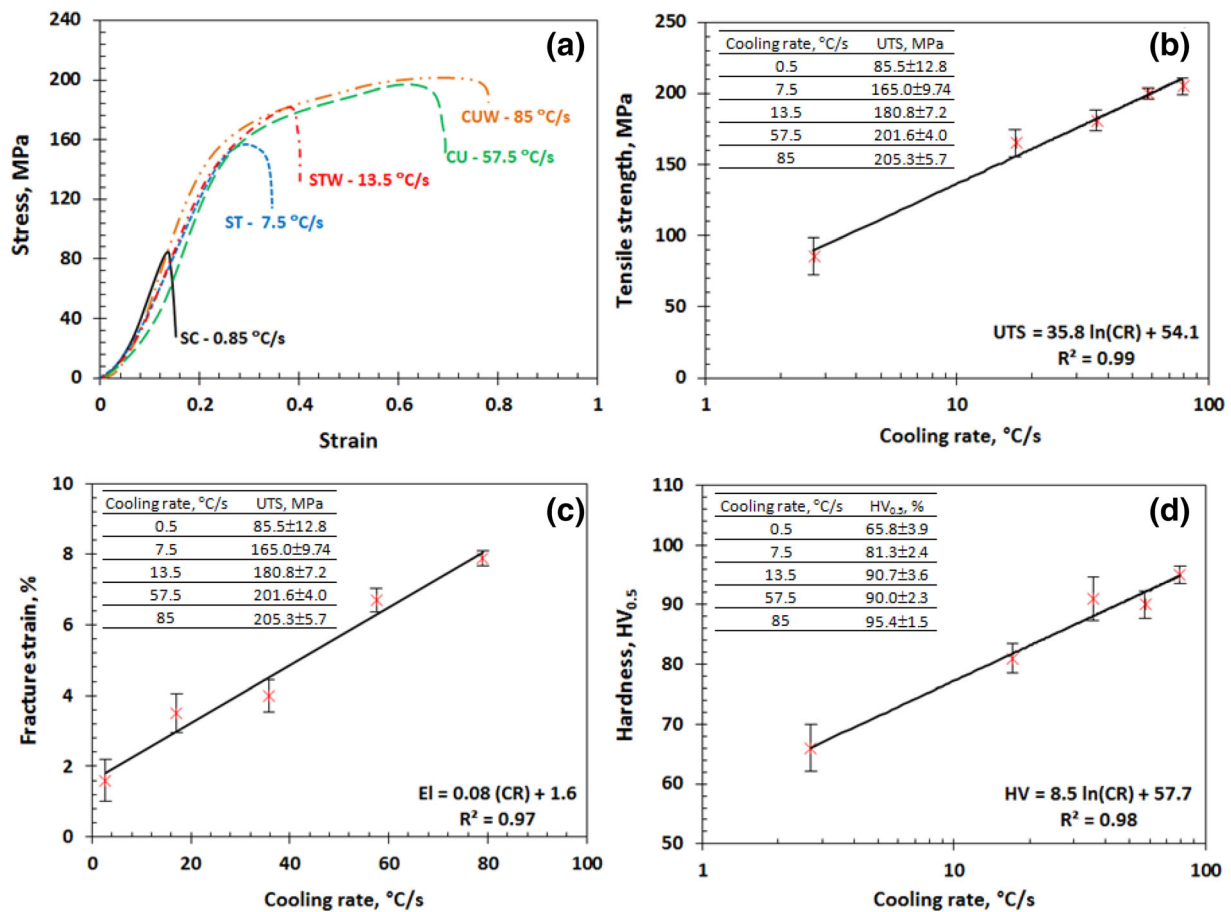


**Figure 7. Effect of cooling rate on the mechanical properties; (a) engineering stress-strain curves, (b) tensile strength, (c) fracture strain, and (d) hardness.**

divided to three regions: (I) primary phase nucleation, (II) pre-eutectic freezing zone, and (III) eutectic phase formation, where the intersection between the dashed borderlines and the cooling curve provides information on time and temperature ranges within the mentioned areas. At high cooling rates (CU and CUW), due to an ultrafast heat extraction from the solidifying system and a small portion of latent heat released during the formation of last eutectic phase, region (III) is not detectable, and consequently, areas (II) and (III) are overlapped with no exact ending border. However, it has been reported that an increase in cooling rate reduces the solidus temperature.<sup>36</sup> A decrease in nucleation temperature of the primary phase as the cooling rate enhances is also observed in these subfigures when the liquidus line is deviated from the equilibrium condition toward lower values. However, due to an intrinsically high diffusion rate in the liquid, this reduction in N value is insignificant (almost 13.9 °C from 0.5 °C/s to 85 °C/s cooling rate transition).

Through region (I), the Al<sub>3</sub>Fe phase starts to nucleate and grow, where the latent heat released during its formation results in more positive values of first derivative axis. Engler et al.<sup>37</sup> also observed Al<sub>3</sub>Fe primary phase in 5xxx aluminum alloys based on thermodynamic simulation.

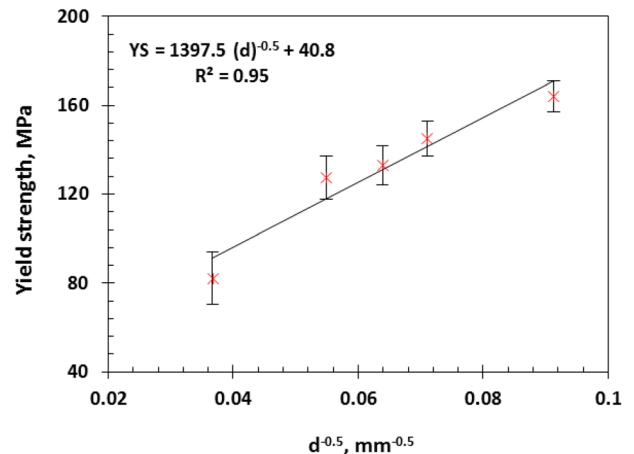


**Figure 8. Variation of yield strength against inverse square root of the average grain size (d).**

Region (II) covers a wide time range within which the pre-eutectic phases of Mg<sub>2</sub>Si and Al<sub>3</sub>Mg<sub>2</sub> form, as an evolution in Al-rich matrix formation is in progress. Finally, in region (III), the eutectic phase of Mg<sub>2</sub>Si nucleates from a very small portion of liquid phase only left behind the interdendritic regions. A sharp increase in cooling rate drastically tightens the solidification time range, refining



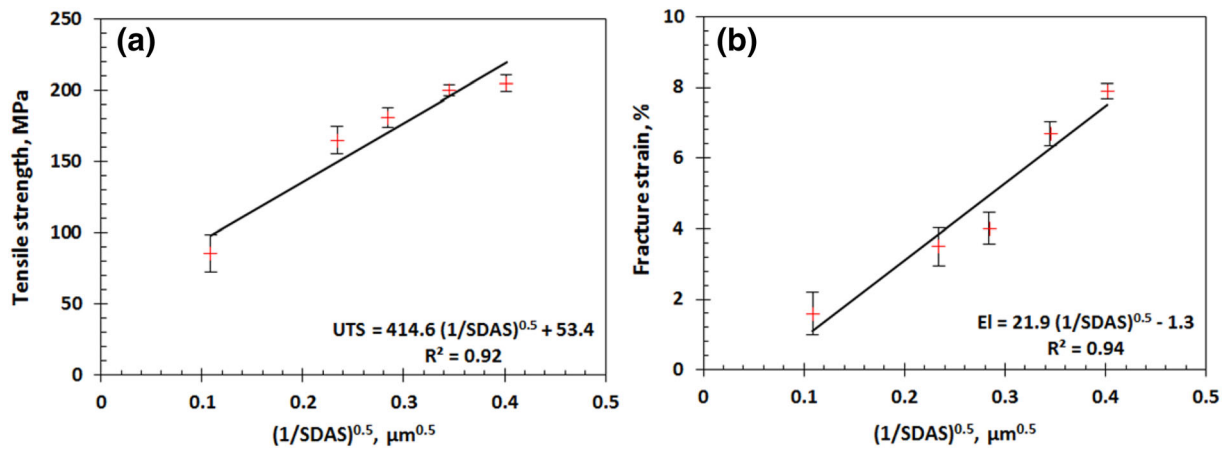


Figure 9. Variation of (a) tensile strength and (b) fracture strain against SDAS for AA5056 alloy.

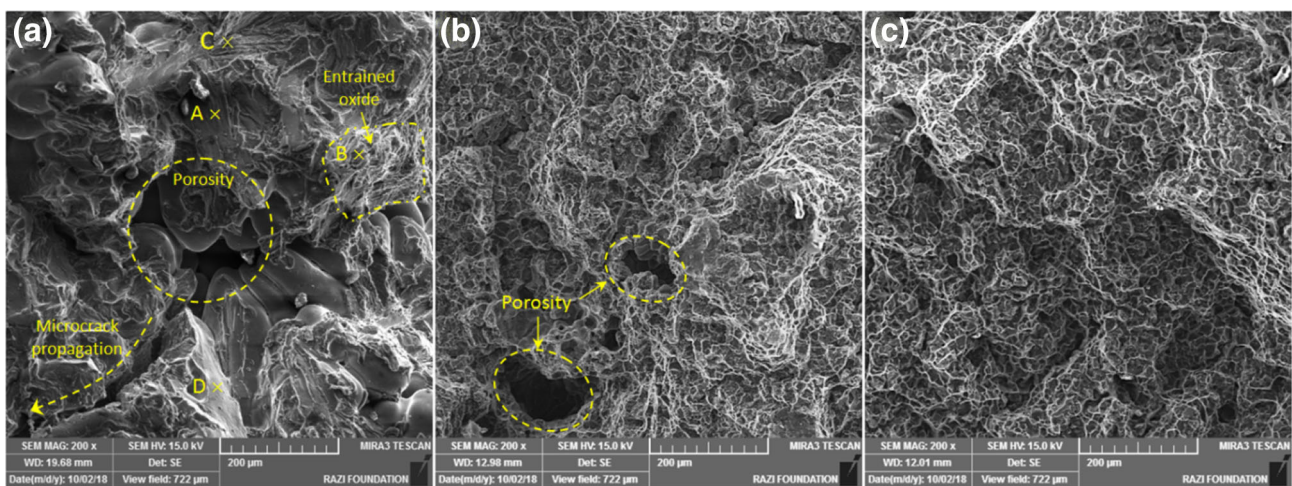


Figure 10. Fracture surface morphology of (a) SC (0.5 °C/s), (b) ST (7.5 °C/s), and (c) CUW (85 °C/s) samples.

both grains and intermetallics due to high thermal undercooling (i.e., high nucleation frequency) and inadequate diffusion time (i.e., short diffusion paths of alloying elements).<sup>38</sup>

### Mechanical Properties

The effect of cooling rate on the mechanical properties of AA5056 alloy is shown in Figure 7. As seen, an increase in the cooling rate from 0.5 °C/s to about 85 °C/s enhances the tensile strength, fracture strain, and hardness by 140%, 395%, and 44%, respectively.

Improving the mechanical properties at high-cooling rates can be explained by the refinement of grains (Figure 4a), lower SDAS (Figure 4b), fine and uniform distribution of second phases, such as  $\text{Al}_3\text{Mg}_2$ ,  $\text{Mg}_2\text{Si}$ ,  $\text{Al}_3\text{Fe}$ , as well as microporosities within the matrix (Figure 3), and enhancement of  $\alpha$ -Al matrix solid solution strengthening.

As reported elsewhere,<sup>39</sup> due to the low value of the Hall-Petch constant, the degree of grain size strengthening in Al alloys is lower than what is observed in ferrous alloys. However, among commercial Al alloys, Al-Mg alloys have the highest grain size dependence on the yield strength.<sup>39</sup> Therefore, decreasing the grain size is likely to improve their strength, especially as it also refines the grain boundary compounds/porosities and promotes their more even distribution within the matrix (Figure 3). The Hall-Petch diagram showing the linear relationship between the yield strength and grain size in AA5056 alloy is shown in Figure 8.

Decreasing the SDAS also effectively refines the second phases and porosities formed in numerous and highly-branched interdendritic channels (Figure 3). The  $\text{Al}_3\text{Mg}_2$  (cubic,  $a = 2.824 \text{ nm}$ <sup>40</sup>),  $\text{Mg}_2\text{Si}$  (anti-fluorite cubic,  $a = 0.6338 \text{ nm}$ <sup>41</sup>), and  $\text{Al}_3\text{Fe}$  (orthorhombic,  $a = 74.4 \text{ nm}$ ,  $b = 64.64 \text{ nm}$ ,  $c = 87.79 \text{ nm}$ , and  $\alpha = \beta = \gamma = 90^\circ$ <sup>42</sup>) intermetallic compounds are inherently hard and brittle, and considering their high melting entropy, grow by a weak and sharp faceted-type interface within the matrix.<sup>43</sup> Moreover,



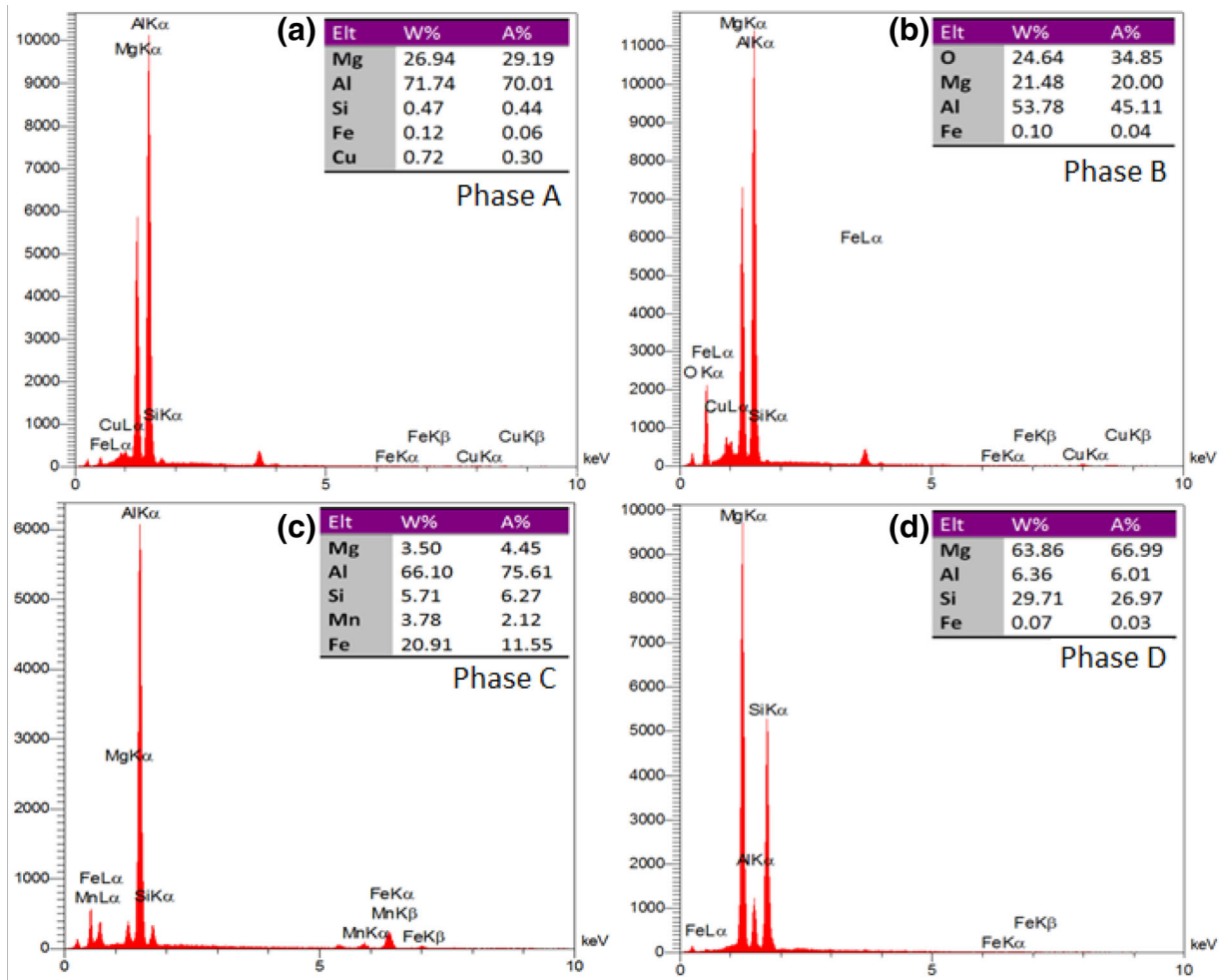


Figure 11. EDS analyses of the phases shown on Figure 10a.

due to the different deformation characteristics, as compared to  $\alpha$ -Al matrix, high stresses are likely to be induced on these particles.<sup>44</sup> Therefore, under the low cooling rate, when they crystallize as rather coarse irregular-shaped particles (Figure 2), the alloy exhibits high microcracking tendency and, consequently, low ductility/formability (Figure 7c). However, the refinement of intermetallics reduces the possibility of defects in their structure<sup>44</sup> and increases their number density, thereby decreasing the amplitude of stress they experience during the tensile loading. This improves their resistance to cracking and/or interfacial de-bonding. However, if microcracks initiate at higher applied loads, small SDAS shortens the microcracks and lowers their linkage tendency through forming shear bands. Under this circumstance, the neighboring microcracks are linked together through ductile failure of intercracks ligaments increasing the material ductility.<sup>45</sup> Improving the particles distribution homogeneity also increases their average interspacing causing the already-initiated microcracks to propagate through the soft Al matrix rather than the cracked particles and/or their weak interfaces.

The fine distribution of micropores also plays a key role in the mechanical properties improvement of the samples prepared under the high cooling rates. This is because the micropores, acting as stress risers/microcrack initiators, decrease the load-bearing cross section of the samples. Decreasing the SDAS has also a positive pronounced effect on the mechanical properties. This is because the small SDASs divide the molten eutectic pockets into many small pockets leading to the finer interdendritic second phases and gas/shrinkage micropores.<sup>44</sup> A regression analysis reveals that the tensile strength and fracture strain of AA5056 alloy are correlated to the size of its SDASs (Figure 9) which is in agreement with the previous studies.<sup>18</sup>

Figure 10 shows the fracture surfaces of SC, ST, and CUW samples. A large porosity is evident on the fracture surface of SC sample. As described before, the porosities act as stress concentrators in the microstructure encouraging the initiation and propagation of microcracks (Figure 10a) and causing the premature fracture of material. In addition to the porosities, the presence of cleavage facets, corresponding to the brittle fracture of  $\text{Al}_3\text{Mg}_2$ ,  $\text{Mg}_2\text{Si}$ , and

Al<sub>3</sub>Fe particles with EDS analyses shown in Figure 11a-d, respectively, and entrained oxides (Figure 10a, point B), imply their critical role in initiation and transgranular propagation of microcracks in SC sample. However, as the cooling rate increases, the density of dendrite cells/grain boundaries also increases, which in turn, reduces the fraction and promotes the fine distribution of second phases/porosities within the matrix (lowering their clustering along dendrite cells and grain boundaries), making the dendrite cells/grains boundaries more discontinuous. Under this condition, the intergranular fracture by formation of small dimples mainly initiated by the fracture of second phases is encouraged (Figure 10b and c).

High cooling rate also promotes solid solution strengthening of  $\alpha$ -Al matrix where its hardness has increased from 60.0±0.5 HV<sub>0.005</sub> in the SC alloy to 62.2±0.9 HV<sub>0.005</sub>, 72.8±0.6 HV<sub>0.005</sub>, and 89.3±3.1 HV<sub>0.005</sub> in the ST, CU, and CUW samples, respectively. This can be explained by the higher distortion of host lattice caused by the higher concentration of solute atoms with atomic radius different from the host Al atoms. The strain fields developed around solutes can impede the movement of dislocations, thereby promoting solid solution strengthening of the matrix.<sup>46,47</sup>

## Conclusions

1. An increase in cooling rate lowers the solidification time range, refining both grains and intermetallics due to high thermal undercooling and inadequate diffusion time. A decrease in nucleation temperature of the primary phase as the cooling rate enhances is also observed when the liquidus line is deviated from the equilibrium condition toward lower values.
2. Increasing the cooling rate from about 0.5 to about 85 °C/s decreased the fraction of Al<sub>3</sub>Mg<sub>2</sub>, Mg<sub>2</sub>Si, and Fe-rich compounds by 58, 64, and 27%, respectively. It also substantially refined the grains, reduced the size of SDAS, and lowered the porosity content from about 3.8% to about 0.3%.
3. An increase in the cooling rate from 0.5 to about 85 °C/s increased the hardness, tensile strength, and fracture strain of the alloy by 44%, 140%, and 395%, respectively.
4. The fractography results revealed that, due to the presence of large porosities and cleavage facets corresponding to the fractured Al<sub>3</sub>Mg<sub>2</sub>, Mg<sub>2</sub>Si, and Al<sub>3</sub>Fe particles, the fracture mechanism changed from a brittle-dominated mode to a high-energy ductile mode comprising of extensive dimpled zones in the samples solidified under the higher cooling rates

**Conflict of interest** The authors had no funding, financial relationships, or conflict of interest to report.

## REFERENCES

1. S.-H. Ha, Y.-O. Yoon, B.-H. Kim, H.-K. Lim, S.K. Kin, et al., *Inter. Metalcast.* **13**, 121 (2019). <https://doi.org/10.1007/s40962-018-0234-3>
2. M. Okayaso, S. Takeuchi, *Int. J. Metalcasting.* **12**, 298 (2017)
3. T. Mukai, M. Kawazoe, K. Higashi, *Nanostruct. Mater.* **10**, 755 (1998)
4. T. Mukai, M. Kawazoe, K. Higashi, *Mater. Sci. Eng. A.* **247**, 270 (1998)
5. K. Prapasajchavet, Y. Harada, S. Kuami, *Inter. Metalcast.* **11**, 123 (2017). <https://doi.org/10.1007/s40962-016-0084-9>
6. G. Li, H. Lu, X. Hu, F. Lin, X. Li, Q. Zhu, *Metals.* **10**, 238 (2020)
7. T. Gong, J. Dong, Z. Shi, X. Yaer, H. Liu, *Mater.* **12**, 4230 (2019)
8. Y. Liu, G. Huang, Y. Sun, L. Zhang, Z. Huang, J. Wang, C. Liu, *Mater.* **9**, 88 (2016)
9. H. Ghandvar, M.H. Idris, T.A. Abu Bakar, A. Nafari, N. Ahmad, *J. Mater: Res. Technol.* **9**, 3272 (2020)
10. J. Campbell, M. Tiryakioğlu, *Mater. Sci. Technol.* **26**, 262 (2010)
11. T. Sheppard, N. Raghunathan, *Mater. Sci. Technol.* **5**, 268 (1989)
12. M. Salarvand, S.M.A. Boutorabi, M. Pourgharibshahi, M. Tamizifar, *Int. J. Metalcasting.* (2021). <https://doi.org/10.1007/s40962-021-00578-8>
13. J.-I. Cho, C.-W. Kim, *Inter. Metalcast.* **8**, 49 (2014). <https://doi.org/10.1007/BF03355571>
14. E. Lee, B. Mishra, *Inter. Metalcast.* **12**, 449 (2018). <https://doi.org/10.1007/s40962-017-0195-y>
15. H.-P. Tang, Q.-D. Wang, C. Lei, B. Ye, K. Wang, H.-Y. Jiang, W.-J. Ding, X.-F. Zhang, Z. Lin, J.-B. Zhang, *J. Alloys Comp.* **801**, 596 (2019)
16. S.S.M. Mehrian, M. Rahsepar, F. Khodabakhshi, A.P. Gerlich, *Surf. Coat. Technol.* **405**, 126647 (2021)
17. P. Snopiński, M. Król, T. Tański, B. Krupińska, *J. Therm. Anal. Calorim.* **133**, 379 (2018)
18. H.-P. Tang, Q.-D. Wang, C. Lei, K. Wang, B. Ye, H.-Y. Jiang, W.-J. Ding, *Acta Metall. Sin. (Eng. Let.)* **32**, 1549 (2019)
19. F.C. Campbell, *Manufacturing Technology for Aerospace Structural Materials*, 1st edn. (Elsevier Ltd., Great Britain, 2006), pp. 391–392
20. J.P. Frick, *Woldman's Engineering Alloys*, 9th edn. (ASM International, Materials Park, OH, 2000)
21. P.J. Morais, B. Gomes, P. Santos, M. Gomes, R. Gradinger, M. Schnall, S. Bozorgi, T. Klein, D. Fleischhacker, P. Warczok, A. Falahati, E. Kozeschnik, *Materials.* **13**, 1610 (2020)
22. R.P. Taylor, S.T. McClain, J.T. Berry, *Int. J. Cast Metals Res.* **11**, 247 (1999)

23. V. Raghavan, *J. Phys. Equil. Diff.* **28**, 213 (2007)
24. G. Liang, Y. Ali, G. You, M.-X. Zhang, *Mater.* **3**, 113 (2018)
25. E. Safary, R. Taghiabadi, M.H. Ghoncheh, *Int. J. Miner. Metall. Mater.* (2021). <https://doi.org/10.1007/s12613-020-2244-4>
26. D.H. St John, M. Qian, M.A. Easton, P. Cao, Z. Hildebrand, *Metall. Mater. Trans. A* **36**(7), 1669 (2005)
27. T. Ahmed, H.X. Jiang, W. Li, J.-Z. Zhao, *Acta Metall. Sinica Eng. Lett.* **31**(8), 842 (2017)
28. G. Liang, Y. Ali, G. You, M.-X. Zhang, *Materialia* **3**, 113 (2018)
29. J. Abboud, J. Mazumder, *Sci. Rep.*, 10(1) (2021)
30. J. Cao, Z. Zeng, F. Zhang, D. Guo, Z. Hou, *Metals* **11**(8), 1291 (2021)
31. O.E. Jegede, N. Haque, A.M. Mullis, R.F. Cochrane, *J. Alloys Comp.* **883**, 160823 (2021)
32. V.A. Hosseini, S.G. Shabestari, R. Gholizadeh, *Mater. Des.* **50**, 7 (2013)
33. N. Haghdadi, A.B. Phillion, D.M. Maijer, *Metall. Mater. Trans. A* **46**(5), 2073 (2015)
34. K.D. Carlson, Z. Lin, C. Beckermann, *Metall. Mater. Trans. B.* **38**, 541 (2007)
35. B. Wang, M. Zhang, J. Wang, *Mater. Today Commun.* **28**, 102524 (2021)
36. S.G. Shabestari, M. Divandari, M.H. Ghoncheh, V. Jamali, *Metall. Mater. Trans. B.* **48**, 2304 (2017)
37. O. Engler, K. Kuhnke, J. Hasenclever, *J. Alloys Compd.* **728**, 669 (2017)
38. M.H. Avazkonandeh-Gharavol, M. Haddad-Sabzevar, H. Fredriksson, *J. Alloys Compd.* **610**, 462 (2014)
39. D.J. Lloyd, S.A. Court, *Mater. Sci. Technol.* **19**, 1349 (2003)
40. M. Kubota, *Mater. Trans.* **46**, 2437 (2005)
41. Y. Li, T. Ma, Y. Ren, T. Liu, X. Zou, *Mater. Res. Express.* **7**, 036 (2020)
42. K. Lee, S. Kumai, *Mater. Trans.* **47**, 1178 (2006)
43. Z. Nouri, R. Taghiabadi, *Trans. Nonferrous Metals Soc. China* **31**(5), 1262 (2021)
44. Q.G. Wang, *Metall. Mater. Trans. A.* **34**, 2887 (2003)
45. Q.G. Wang, C.H. Cáceres, *Mater. Sci. Eng. A* **241**(1–2), 72 (1998)
46. T. Keil, D. Utt, E. Bruder, A. Stukowski, K. Albe, K. Durst, *J. Mater. Res.* **36**(12), 2558 (2021)
47. D. Zhou, X. Ye, J. Teng, C. Li, Y. Li, *Mater.* **14**(3), 656 (2021)

**Publisher's Note** Springer Nature remains neutral with regard to jurisdictional claims in published maps and institutional affiliations.